Hindawi
Mathematical Problems in Engineering
Volume 2019, Article ID 7050151, 15 pages
https://doi.org/10.1155/2019/7050151

Research Article

Dynamic Parameter Analysis of Spindle Bearing Using 3-Dimension Quasi-Dynamic Model

Jie Yu,[1,2] Songsheng Li,[1] Xiaoyang Chen,[1] Lei He,[2] and Wei Yuan[2]

[1]*Shanghai Key Laboratory of Mechanical Automation and Robotics, Shanghai University, Shanghai 200072, China*
[2]*School of Mechanical Engineering, Shandong University of Technology, Zibo 255049, China*

Correspondence should be addressed to Wei Yuan; wyuan16@sdut.edu.cn

Received 20 November 2018; Accepted 8 January 2019; Published 17 January 2019

Academic Editor: Mohammed Nouari

Spindle bearing with high rotational speed is the kernel of many rotating machines which plays massive important role in the performance of the whole machine. There are also some deficiencies of the present quasi-dynamic mathematical models of the rolling bearing in analyzing the bearing dynamic parameters. This paper develops the 3D quasi-dynamic model with ball's 6-DOF, cage's 6-DOF, and driving ring's 5-DOF under steady working stage, based on the analysis of the relative position of each component to determine the normal forces between each component and the analysis of the relative velocity of the contacting point to determine the tangential force between each component. This model can analyze the dynamic parameters, such as the spin-to-roll ratio of inner and outer rings, the angular velocity of rolling elements in y-axis of the location coordinate, the normal contact force of cage pocket and ball, the cage angular velocity and ball revolution velocity, and the gyroscopic moment under different working condition. Compared with the numerical calculation results of ADORE program, the results of the proposed model are able to accurately describe the change laws of the spindle bearing parameters.

1. Introduction

Development of a spindle bearing system can significantly improve the efficiency and accuracy of machine tools. The quasi-dynamic models of the spindle bearing are not only better capable of analyzing bearing dynamic parameters than quasi-static models and could also need less numerical calculation time than the dynamic model. Generally, the steady working duration of ball bearings would last 90 percent of the whole service life under normal condition. Therefore, establishment of perfect bearing quasi-dynamic model plays massive significant role on the analysis of the bearing operational performance [1–3], such as cage slipping, cage impacts, roller skidding, roller-flange contact, and roller skewing.

Many contributions for spindle bearing system were conducted based on the bearing quasi-dynamic modeling, such as Harris [4] and Yuan [5], who established the equation groups about 6 degrees of rolling elements, 3 degrees of cages, and 5 degrees of rings by dropping the hypothesis of the ring control theory and considering the oil film drags of the contacting ellipse between rolling elements and raceways with oil film lubrication. Wang et al. [6] analyzed the boundary conditions of aeroengine bearing by the quasi-dynamic method and then discussed the relationship between status parameters associated with Failure modes (such as lubricating oil film thickness, etc.) and working parameters (such as rotation speed and external load). Ren et al. [7] established a new quasi-dynamic model of the counter-rotating cylindrical roller bearing based on elastohydrodynamic lubrication theory, hydrodynamic lubrication theory, and the quasi-dynamic analysis method to dynamic behaviors of counter-rotating cylindrical roller bearing. However, those researches have not considered the complete degree of freedom of the rolling bearing components which is very significant to determine their dynamic characteristics. Therefore, it is badly necessary to establish the bearing quasi-dynamic model for the analysis of the component complete degree of freedom.

In order to reflect the real operation of high speed angular contact ball bearings, a quasi-dynamic calculation model for the high speed angular contact ball bearing was built by embedded Broyden-Fletcher-GoldFarb-Shanno mutative

scale optimization in quasi-dynamic calculation program [8]. For the spindle bearing with a certain contact angle, gyroscopic moment will inevitably induct large sliding between the balls and raceways and increase the bearing friction moment, which are the main reasons for the bearing heat generation and wear [9–11]. Therefore, accurately analyzing the spin angular velocity between ball and raceway is benefit for the correct calculation of bearing power dissipation, assessment of the rate of heat generation, and appropriate decision of lubrication flow rate, etc. Meanwhile, the bearing cage is a critical component which is often the most Failure part for high speed bearings, typically. With the increase of bearing rotation speed, the analytical precision of the contact force between the cage and the balls or the guide rings is dramatically important for the force characteristics of bearing research [12–14].

To analyze the operating characteristics of rolling bearings at steady working stage, the bearing quasi-dynamic model is developed in this paper. In the optimal model, (i) by the analysis of the relative positions of each bearing component, the normal forces between the bearing components are determined and (ii) the tangential forces between the bearing components are obtained according the study of the directions and magnitudes of the relative velocities of the contact points and then (iii) the force mathematical models of balls' 6-DOF, cage's 6-DOF, and the driving ring's 5-DOF. On the base of those models, the gyroscopic moment model is established to analyze the pitching angles and yaw angles, and the cage forces and operating condition are studied by the contacting force models between the cage and the ball and guide ring. The results of the improved quasi-dynamic model are furthermore compared with the results of the typical rolling bearing force calculation example of Gupta [15]. Studies show that the model is able to accurately describe the dynamic variations of the parameter characteristics of spindle bearings.

2. Mechanics Modeling of Spindle Bearing

2.1. Techniques of Mechanics Modeling. Figure 1 shows the interaction model of bearing components. The interaction forces between these parts are mainly the normal contact forces and the tangential forces. First, by means of determining the position vectors of part B and part A in space, judging whether part B in contact with part A and calculating the normal contact force, the normal force of part B relative to part A can be obtained. Second, according to the velocity vectors of part A and part B in space, the velocity direction of part B relative to part A at the contact point can be determined, and on the basic of Coulomb's law, the tangential force of part B relative to part A is obtained. Finally, the influence of the lubricant on the force will be considered to solve the force of part B relative to part A. Equilibrium equations of part A and part B will be established and the numerical solution can be done by considering these three factors.

2.2. Interaction Model of Each Parts of Bearing

2.2.1. Interaction of Ball and Ring. The vector position relationship of ball and ring in space is shown in Figure 2. The points of O_i and O_e are the centers of inner and outer raceway groove curvatures, respectively. The position vectors of $\boldsymbol{r}_{boe}$ and $\boldsymbol{r}_{boei}$ are from the center of the ball to the centers of groove curvature of the outer ring and the inner ring, respectively.

In the vector triangle of ΔOO^aO_e (seeing Figure 2), the vector of $\boldsymbol{r}_{boe}$ is the position vector from the ball center to the outer raceway groove curvature center and can be expressed by

$$r_{boe} = r_b - r_{Ooe} \tag{1}$$

Likewise, the vector of $\boldsymbol{r}_{boe}$ in the vector triangle of $\Delta O^rO^aO_i$ is the position vector from the ball center to the inner raceway groove curvature center and can be described as

$$r_{boi} = r_b - r_{Ooi} \tag{2}$$

The elastic approaches of ball and ring raceways are expressed by

$$\delta_k = r_{bok} - \left(f_k - 0.5\right) d_w \tag{3}$$

where $k = i, e$ denote the inner and outer ring, respectively. When $\delta_k \le 0$, the ball and raceway have no contact with each other and contact deformation will not occur, and the normal force is zero, whereas when $\delta_k > 0$, the contact deformation occurred, and the normal contact load can be obtained by (4) using Hertz theory of contact stress.

$$F_{kH} = K\delta_k \tag{4}$$

where k is the stiffness coefficient of Hertz contact.

As illustrated in Figure 3, the local coordinate of o_xy is established to analyze the contact ellipse between ball and inner raceway. Relative linear velocity can be described in the direction of x-axis and y-axis as (5) and (6), respectively.

$$V_{xi} = -\left\{\sqrt{{R_i}^2 - {x_i}^2} - \sqrt{{R_i}^2 - {a_i}^2} + \sqrt{\left(\frac{d_w}{2}\right)^2 - {a_i}^2}\right\} \cdot \omega_i \left(\frac{\omega_b}{\omega_i}\right) \cos\beta \sin\beta' \tag{5}$$

$$V_{yi} = -\frac{\omega_i}{2} D_m - \left\{\sqrt{{R_i}^2 - {x_i}^2} - \sqrt{{R_i}^2 - {a_i}^2} + \sqrt{\left(\frac{d_w}{2}\right)^2 - {a_i}^2}\right\} \times \left(\frac{\omega_b}{\omega_i} \cos\beta \cos\beta' \cos\alpha_i + \frac{\omega_b}{\omega_i} \sin\beta \sin\alpha_i - \cos\alpha_i\right) \omega_i \tag{6}$$

The angle between the direction of relative linear velocity and the direction of semimajor axis of the contact ellipse is

$$\vartheta_{br} = \arctan\left(\frac{-V_{xi}}{V_{yi}}\right) \tag{7}$$

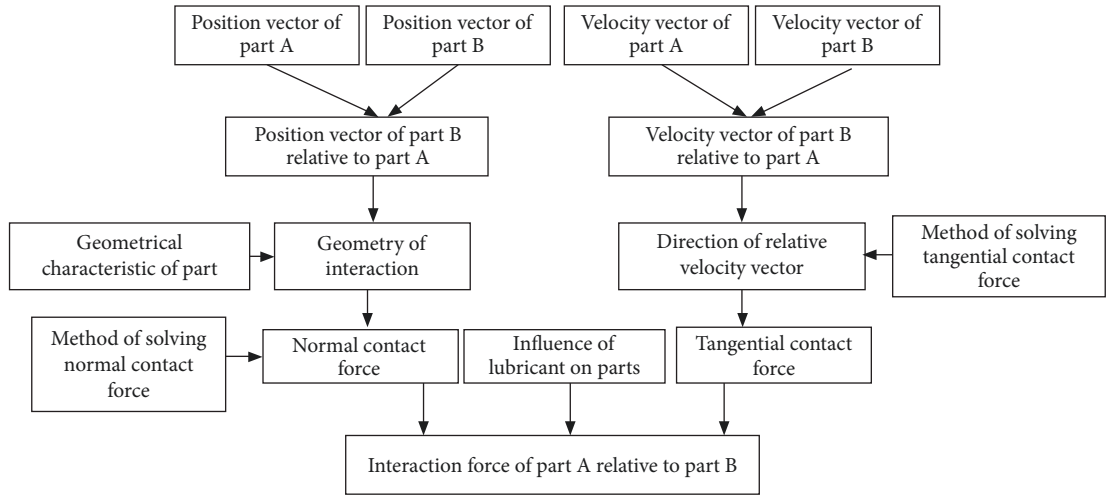

Figure 1: Interaction model of each part in the bearing.

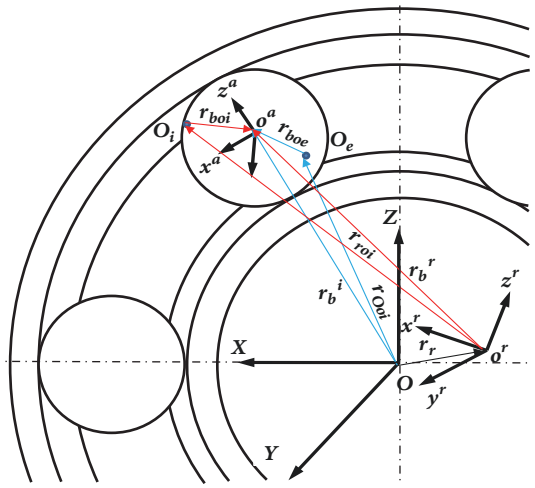

Figure 2: Geometric relationship of balls and ring.

According to Coulomb's law, tangential friction with respect to semimajor axis and semiminor axis of the contact ellipse is stated as

$$T_{ix} = -T_i \sin \vartheta_{br}$$
$$T_{iy} = T_i \cos \vartheta_{br} \tag{8}$$

The force of contact point between ball and inner raceway is then obtained as

$$F_i = \left[\mathrm{T}_{ix}, \mathrm{T}_{iy}, \mathrm{F}_{iH}\right] \tag{9}$$

As illustrated by Figure 4, the vectors from the ball center to the contact ellipse centers of inner and outer raceways are $\boldsymbol{r}_{obi}$ and $\boldsymbol{r}_{obe}$, respectively. The friction torque between the ball and the inner raceway is as follows:

$$M_{bri} = r_{obi} \times \left[\mathrm{T}_{ix}, \mathrm{T}_{iy}, 0\right] \tag{10}$$

and the friction torque of the inner raceway is

$$M_{rbi} = \left(r_{obe} + r_{ori}\right) \times \left[\mathrm{T}_{ix}, \mathrm{T}_{iy}, 0\right] \tag{11}$$

where $\boldsymbol{r}_{ori}$ is the vector from the ball center to inner ring coordinate center. Similarly, the contact force between ball and outer raceway can be given as

$$F_e = \left[\mathrm{T}_{ex}, \mathrm{T}_{ey}, \mathrm{F}_{eH}\right] \tag{12}$$

2.2.2. Interaction of Ball and Cage. As illustrated in Figure 5, the vectors of r_{bp1}^p and r_{bp2}^p are the first and the second components of the vectors from the ball center to the cage pocket center in the pocket coordinates $o^p\_x^p y^p z^p$, respectively. The contact point between the ball and the pocket wall and the ball center and the pocket center is aligned in line. The minimum distance from pocket wall to the ball surFace can be expressed as

$$\delta_{bp} = \frac{d_p - d_w}{2} - \sqrt{\left(r_{bp1}^p\right)^2 + \left(r_{bp2}^p\right)^2} \tag{13}$$

When $\delta_{bp} \le 0$, the elastohydrodynamic lubrication state will occur between the ball and cage pocket, and the normal force component between the ball and cage in the contact coordinate system can be obtained based on Brewe formula by [16]

$$F_{bp} = \frac{UL}{\varphi}\sqrt{\frac{128\alpha_r R_z}{h}} \tag{14}$$

where $L = 0.131 \arctan(\alpha_r/2) + 1.683$, $\varphi = (1 + 2/3\alpha_r)^{-1}$, and $\alpha_r = R_x/R_z$ $U = \eta_o u/E' R_z$. And the corresponding tangential force component can be given using Coulomb Law as follows:

$$T_{bc} = \mu_{bp}\left|F_{bp}\right| \tag{15}$$

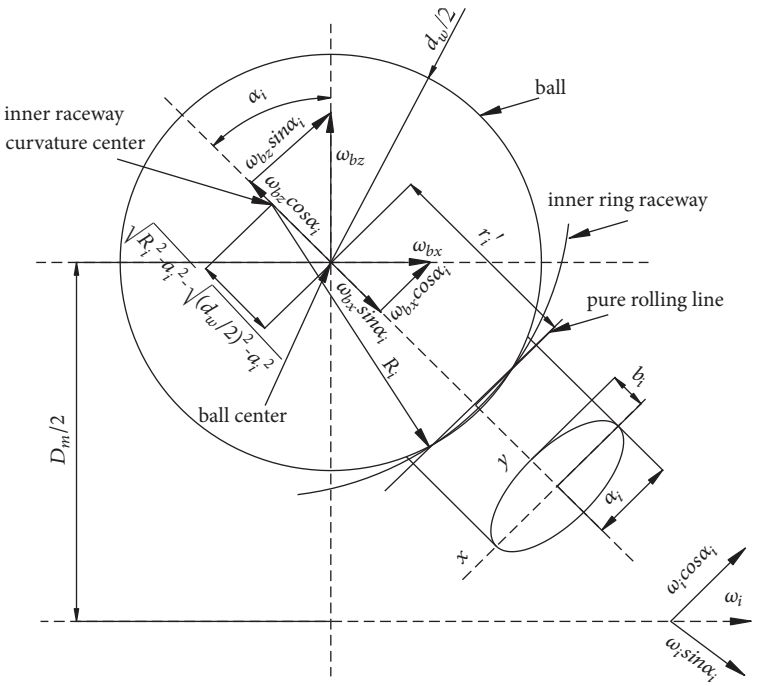

Figure 3: Contact feature of ball and inner raceways.

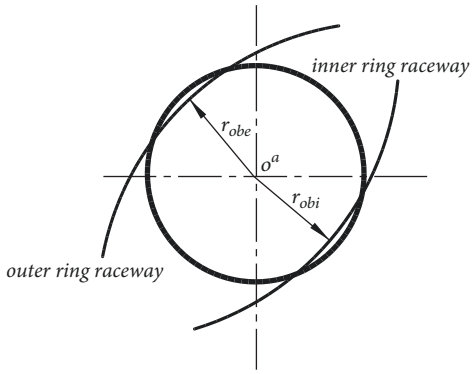

Figure 4: Relative position between the ball center and the inner and outer raceway.

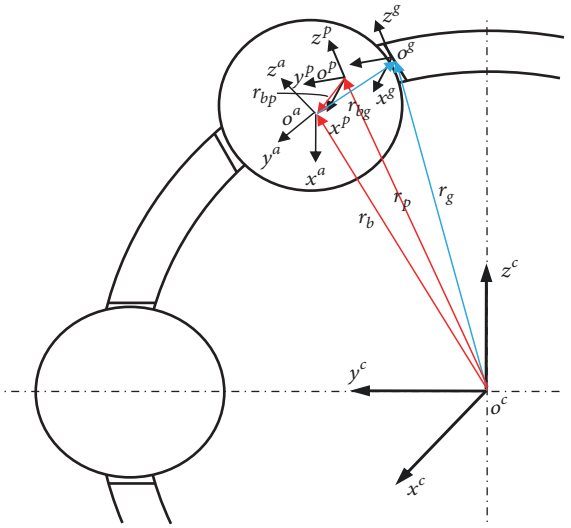

Figure 5: Geometric relationship of balls and cage.

where R_x is the equivalent radius along semimajor axis of the contact area in the contact coordinate, R_z is the equivalent radius along semiminor axis of the contact area in the contact coordinate, η_0 is the dynamic viscosity of lubricating oil, u is the relative sliding speed of the ball and the pocket wall, E' is the equivalent elastic modulus of the ball and the cage, and μ_{bp} of 0.02 ~ 0.08 is the friction coefficient between the ball and the pocket wall.

When $\delta_{bp} < 0$, contact deformation will occur between the ball and the pocket wall, and the normal contact load can be obtained by using Hertz theory as

$$F_{bp} = K_c \left(\delta_{bp}\right)^{3/2} \tag{16}$$

The relative line velocity at the contact point of the ball and the pocket wall is

$$v_{bp} = v_{gb} - v_{gp} \tag{17}$$

In contact coordinate $o^g\_x^g y^g z^g$, the angle between v_{bp} with z^g axis is

$$\vartheta_{bp} = \operatorname{acrtan}\left(\frac{v_{bp1}}{v_{bp3}}\right) \tag{18}$$

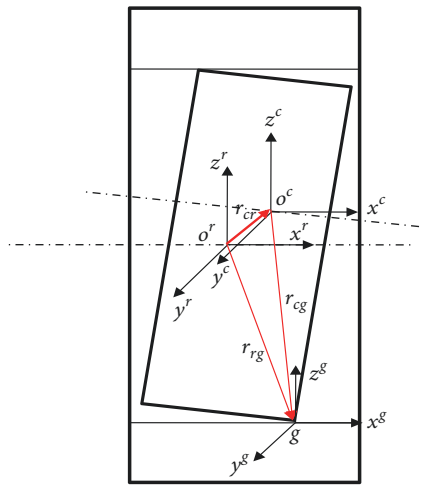

Figure 6: Geometric relationship of cage and guide ring.

The tangential friction forces along the directions of x^g and z^g are expressed as follows, respectively:

$$T_{bcx} = T_{bc} \sin \vartheta_{bp}$$
$$T_{bcz} = T_{bc} \cos \vartheta_{bp} \tag{19}$$

The force and the moment subjected to the ball by cage pocket can be stated as follows, respectively:

$$F_{bc} = \left[\mathrm{T}_{bcx}, F_{bpn}, \mathrm{T}_{bcz}\right]^T \tag{20}$$

$$M_{bc} = r_{gb} \times F_{bc} \tag{21}$$

According to Newton's third law, the force and the moment subjected to the cage by the ball can be obtained as follows, respectively:

$$F_{cb} = -F_{bc} \tag{22}$$

$$M_{cb} = \left(r_{gp} + r_{pc}\right) \times F_{cb} \tag{23}$$

where $\boldsymbol{r}_{gp}$ is the position vector from the contact point of ball and pocket wall to the pocket center and $\boldsymbol{r}_{pc}$ is the position vector from the pocket center to the cage coordinate center.

2.2.3. Interaction of Cage and Guide Ring. Because of the effect of inertial force during steadily working process, the cage and guide ring exist potential collision, which can be assessed by the minimum clearance between the cage and the guide ring. As shown in Figure 6, the minimum clearance in the vector triangle $\Delta O_r O_{cg}$ is given as

$$\delta_{rc} = \pm\left(R_r - \sqrt{\left(r^r_{rg2}\right)^2 + \left(r^r_{rg3}\right)^2}\right) \tag{24}$$

where the symbols "+" and "-" are for outer and inner guide rings, respectively. r^r_{rg2} and r^r_{rg3} are the second and third components of r^r_{rg}, respectively, which is the vector from the guide ring center to contact point of cage and ring in ring coordinate system $o^r\_x^r y^r z^r$.

When $\delta_{rc} \le 0$, hydrodynamic lubrication will occur between the cage and the guide ring, and the interaction condition can be regarded as short sliding bearing. In the contact coordinate system $o^g\_x^g y^g z^g$ (seeing in Figure 5), the interaction forces of each direction are calculated by the following formula [17, 18]:

$$F^g_{crx} = -\frac{2\pi\eta V^g_{crx} R_c^2 B_c}{C_g}$$
$$F^g_{cry} = \pm\frac{\pi\eta\,|u|\,B_c^3\varepsilon}{4C_g^2\left(1-\varepsilon^2\right)^{3/2}} \tag{25}$$
$$F^g_{crz} = \pm\frac{\eta u B_c^3 \varepsilon^2}{C_g^2\left(1-\varepsilon^2\right)^2}$$

where V^g_{crx} is the relative speed of the cage with respect to the guide ring at the minimum clearance in the direction of x^{g} axis, B_c is the width of the cage, u is drag speed of lubricating oil, $u=R_{\mathrm{c}}(\omega_r+\omega_c)$, C_g is the cage guide clearance, and ε is relative offset of the cage center.

$$\varepsilon = \frac{e}{C_g}$$
$$e = \sqrt{(x^c)^2 + (y^c)^2 + (z^c)^2} \tag{26}$$

The friction moment of the moving cage caused by distribution pressure of fluid pressure oil film can be expressed as

$$M^c_{crx} = \frac{2\pi\eta V_{cr} R^2_{gc} B_c}{C_g\sqrt{1-\varepsilon^2}} \tag{27}$$

where $\boldsymbol{V}_{cr}$ is the relative sliding speed of the cage rail with respect to the ring land and can be stated as follows:

$$V^g_{cr} = R_c\left(w_r - w_c\right) \tag{28}$$

When $\delta_{rc} > 0$, contact deformation will occur between the cage and the guide ring, and the normal contact load can be obtained by using Hertz theory as

$$F^g_{crz} = K_l \delta^{10/9}_{rc} \tag{29}$$

where K_l is the Hertz contact stiffness coefficient with finite length.

The relative sliding speed of the ring with respect to the cage at contact point is

$$v_{rc} = v_{rg} - v_{cg} \tag{30}$$

where $\boldsymbol{v}_{rg}$ is the velocity at the contact point of the ring and $\boldsymbol{v}_{cg}$ is the velocity at the contact point of the cage. $\boldsymbol{v}_{\mathrm{rc1}}$ and $\boldsymbol{v}_{\mathrm{rc2}}$ are the first and second components of the tangential relative velocity, respectively, and the angel along x^{g} axis is

$$\vartheta_{cr} = \arctan\left(\frac{v_{rc2}}{v_{rc1}}\right) \tag{31}$$

Applying Coulomb's law, the tangential force at the contact point is

$$F_{cr} = \mu_{cr} F_{crz} \tag{32}$$

where u_{cr} is the friction coefficient between the cage and the guide ring and is set 0.02 ~ 0.08.

The tangential forces in the direction of x^{g} and y^{g} axis of the contact coordinate $o^{\mathrm{g}}\_x^{\mathrm{g}} y^{\mathrm{g}} z^{\mathrm{g}}$ are as follows, respectively:

$$\begin{aligned} T_{crx} &= T_{cr} \cos \vartheta_{cr} \\ T_{cry} &= T_{cr} \sin \vartheta_{cr} \end{aligned} \tag{33}$$

According to Newton's third law, the force and the moment of the cage caused by the guide ring are

$$\begin{aligned} F_{cr} &= \left[\mathrm{T}_{crx}, T_{cry}, F_{crz} \right] \\ M_{cr} &= r_{gc} \times F_{cr} \end{aligned} \tag{34}$$

where $\boldsymbol{r}_{gc}$ is the vector distance from the center of cage coordinate system to the contact point between the cage and the ring.

2.2.4. Drag of Ball from Oil-Gas Mixture. The balls should overcome the viscous friction drag caused by the bearing internal lubrication during orbital motion. The viscous friction drag of a ball shown in [19] can be approximately expressed by

$$F_d = \frac{\rho_{ef} \pi C_D d_w^2}{32g} \left(D_m \omega_m \right)^{1.95} \tag{35}$$

where ρ_{ef} is the lubricant density in the bearing free space divided by the volume of the free space and the drag coefficients C_D can be determined from [20].

2.3. The Establishment of Equilibrium Equations. The equilibrium equations of the ball are established in the azimuth coordinate system of the ball, in which there are six unknown parameters that need to be calculated, and they are x_b, r_b, ω_m, ω_{bx}, ω_{by}, and ω_{bz}.

The inertial forces on a ball are

$$\begin{aligned} F_x &= 0 \\ F_y &= m_b a_y = m_b \dot{\omega}_m r_b \\ F_y &= m_b a_z = m_b \omega_m r_b^2 \end{aligned} \tag{36}$$

and the inertial moments on a ball are

$$\begin{aligned} M_x &= -I_b \dot{\omega}_{bx} \\ M_y &= -I_b \left(\dot{\omega}_{by} + \omega_m \omega_{bz} \right) \\ M_z &= -I_b \left(\dot{\omega}_{bz} - \omega_m \omega_{by} \right) \end{aligned} \tag{37}$$

where I_b is the inertia moment and can be calculated by $I_b = m_b d_w^2 / 10$.

The equilibrium equations of ball's force and moment are

$$F_{br1}^a + F_{bc1}^a = 0 \tag{38}$$

$$F_{br2}^a + F_{bc2}^a + F_d + F_y = 0 \tag{39}$$

$$F_{br3}^a + F_{bc3}^a + F_z = 0 \tag{40}$$

$$M_{br1}^a + M_{bc1}^a + M_x = 0 \tag{41}$$

$$M_{br2}^a + M_{bc2}^a + M_y = 0 \tag{42}$$

$$M_{br2}^a + M_{bc2}^a + M_y = 0 \tag{43}$$

The force equilibrium equations of the cage are established in the inertial coordinate system of the bearing, and the moment equilibrium equation are established in the fixed coordinate system of the cage. There are the six parameters need to be determined as x_{c}, y_{c}, z_{c}, ω_{cx} θ_{cy}, and θ_{cz}.

The force and moment equilibrium equations of the cage are

$$F_{cr1}^i + F_{cb1}^i = 0 \tag{44}$$

$$F_{cr2}^i + F_{cb2}^i = 0 \tag{45}$$

$$F_{cr3}^i + F_{cb3}^i = 0 \tag{46}$$

$$M_{cr1}^c + M_{cb1}^c = 0 \tag{47}$$

$$M_{cr2}^c + M_{cb2}^c = 0 \tag{48}$$

$$M_{cr3}^c + M_{cb3}^c = 0 \tag{49}$$

The force equilibrium equations of the guide ring are established in the inertial coordinate system of the bearing, and the moment equilibrium equations are established in the ring fixed coordinate system. Similarly, there are also six parameters need to be solved x_{r}, y_{r}, z_{r}, θ_{ry}, θ_{rz}. The force and moment equilibrium equations of the guide ring are

$$\begin{aligned} F_x - \sum_{j=1}^{z} \left(F_{rcj1}^i + F_{rbj1}^i \right) &= 0 \\ F_y - \sum_{j=1}^{z} \left(F_{rcj2}^i + F_{rbj2}^i \right) &= 0 \\ F_z - \sum_{j=1}^{z} \left(F_{rcj3}^i + F_{rbj3}^i \right) &= 0 \\ M_y - \sum_{j=1}^{z} \left(M_{rc2}^r + M_{rb2}^r \right) &= 0 \\ M_z - \sum_{j=1}^{z} \left(M_{rc3}^r + M_{rb3}^r \right) &= 0 \end{aligned} \tag{50}$$

2.4. Numerical Solution. In this paper, six equations of the ball and cage and five equations of the guide ring were solved numerically by Matlab tools. The magnitude order of the

displacement and angular velocity is significantly different; therefore, it is easy to get a nonconvergent solution by combining them to solve. In order to solve this problem, the method from first partial to whole is adopted in this paper. The displacement variables are determined first, and then the angular velocity variables are calculated. Thereafter, the initial value, the displacement, and angular velocity variables will be solved together. The solution process is shown in Figure 7.

3. Validation

In order to verify the accuracy of the updated mathematical model of the angular contact ball bearing, the results of a typical example is illustrated to compare the results with ADORE calculation. The values of bearing parameters are listed in Table 1.

Bearings working condition is set as F_a of 2000 N, F_{r} of 400 N, *ni* of 120000 r/min with the fixed outer ring. Comparing the results of this paper's program with Gupta's ADORE dynamics program at 12.87 ms, the results are compared in Table 2.

As listed in Table 2, the results of this paper and Gupta's show that the maximum error is about 10%. Such phenomenon is due to the fact that (i) the interference fit generated by bearing installed on the spindle was not considered, which would lead the initial contact angle to decrease, (ii) Gupta's ADORE dynamics program considered the acceleration influence, but the proposed mechanical model of ball bearing in this paper did not considered such factor.

Table 1: Geometry parameters of ball bearing.

Bearing parameters	value
Pitch diameter(mm)	31
Ball diameter(mm)	8
The number of balls	6
Initial contact angle(°)	24
Inner rolling groove curvature	0.56
outer rolling groove curvature	0.52
Bearing bore diameter(mm)	20
Bearing outside diameter (mm)	42
Cage outside diameter(mm)	35
Cage core diameter (mm)	30
Cage width(mm)	14
Elasticity modulus (MPa)	2e5

4. Dynamic Analysis of Spindle Bearing

4.1. Influence of Working Condition Parameters. The changes of F_a, F_r, and *ni* have significant influence on the dynamic characteristics of bearing. Based on the variation of these three working conditions (Table 3), the variation rule of bearing dynamic parameters is analyzed.

4.1.1. Influence of Working Conditions on the Spin-To-Roll Ratio. As an important parameter of the angular contact bearing at high speed, spin-to-roll ratio represents the state of the ball rolling in the raceway. Friction and heating are produced during the spinning of the raceway relative to the ball, and the rotation sliding is more serious with large spin-to-roll ratio, which will lead to the severe heat and wear. Therefore, the spin-to-roll ratio should be reduced as much as possible during operation. The change rule of spin-to-roll ratio is analyzed under three working conditions as tabulated in Table 3.

Figures 8 and 9 show that the variations of the spin-to-roll ratio of ball- inner and ball-outer raceway with the change of F_a. It can be illustrated that (i) the spin-to-roll ratio of the ball-inner raceway is much larger than that of the ball-outer raceway under the constant F_r and *ni*, (ii) the ball-raceway spin-to-roll ratio decreases with the increase of F_a, and such phenomena are due to the fact that F_a can reduce axial clearance and the spin angular velocity of the ball-inner and ball-outer raceways and increase the spindle bearing axial preload, which will result in spin-to-roll ratio lower, (iii) the ball spin-to-roll ratio is different at any ball azimuth location with the influence of F_r, (iv) there exists a certain spin-to-roll ratio between the ball and the outer raceway, which indicates that the high speed spindle bearing of oil lubrication does not conform to the hypothesis of outer raceway control, and (v) when F_a=1000 N and F_a=1500 N, the ball at the location angle of 120° has the maximum spin-to-roll ratio; with the increase of the load, the spin-to-roll ratio of the ball in this position gradually becomes the minimum. The reason for this phenomenon is that when bearing axial load is relatively small, there is axial clearance between ball and outer ring, which cannot make the ball press outer ring tightly that results in high spin angular velocity.

Figures 10 and 11 show the variation curves of the spin-to-roll ratio of ball-inner and ball-outer raceways with respect to the radial load. Results show that, with constant F_a and *ni*, the spin-to-roll ratio of the ball-inner raceway decreases in the loading area and increases in the nonloading area, because the radial load can decrease the radial clearance in the loading area and then the ball and the raceway are tightly pressed, which resulted in the spin-to-roll ratio reducing. On the contrary, the spin-to-roll ratio will increase in the nonloading area. It also can be found that the radial load has less effect on the spin-to-roll ratio of the ball-outer raceway than of the ball-inner raceway.

As shown in Figures 12 and 13, under the constant loads F_a and F_r, the spin-to-roll ratio of the ball-inner raceway increases obviously with *ni* increase; comparatively, the spin-to-roll ratio of the ball-outer raceway increases gradually. Such phenomena are due to the fact that the centrifugal force increased with *ni* increasing, which leads to the decrease of the contact load of the ball-inner raceway and the increase of the sliding of the ball-inner raceway and the spin-to-roll ratio obviously. The increase of the centrifugal force can also increase the contact load of the ball and the raceway, restrain the sliding between the ball and the raceway, and slow down the spin-to-roll ratio increase. The ball at location angle of 120° has the maximum spin-to roll ratio with the inner ring and the minimum spin-to-roll ratio with the outer ring; the

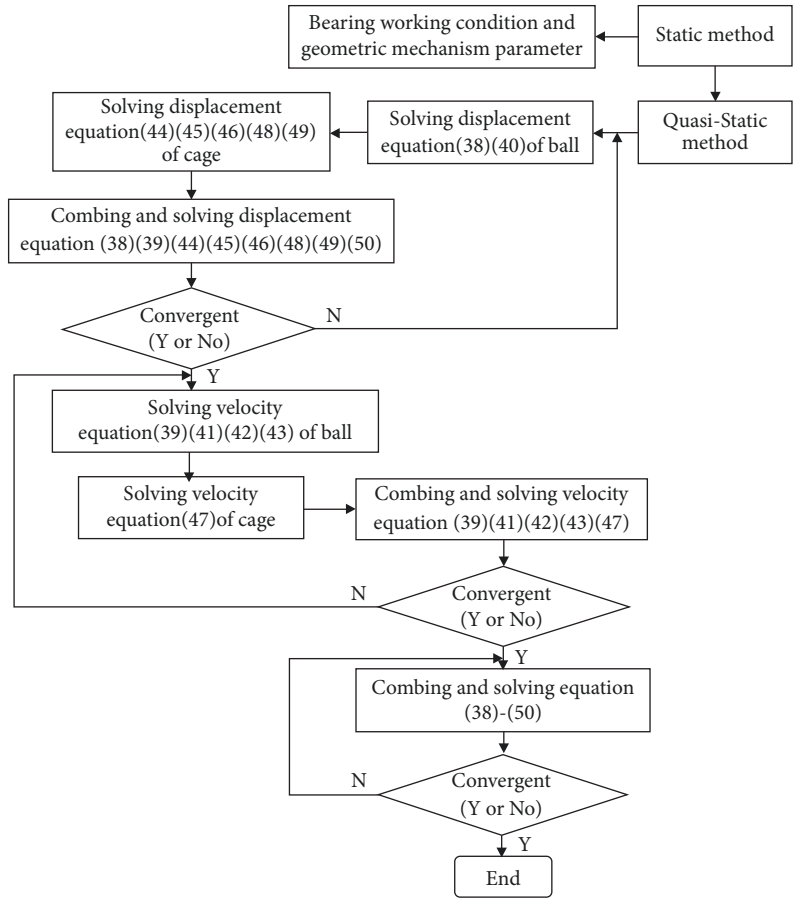

Figure 7: Numerical calculation flow chart.

Table 2: Comparison of the computation results at 12.87ms.

Calculating parameter	The result of Gupta	The result of this paper
Contact angle of ball and inner ring(°)	28.29	33.20
Contact angle of ball and outer ring (°)	13.87	14.14
Maximum contact stress of ball and inner ring (Gpa)	2.799	2.883
Maximum contact stress of ball and outer ring (Gpa)	2.253	2.308
Semi-major axis of the contact area of ball and inner ring (mm)	0.7971	0.8018
Semi-major axis of the contact area of ball and outer ring (mm)	1.478	1.512
Spin-to-roll ratio of ball and inner ring	0.3482	0.4072
Revolution velocity of ball(r/min)	46660	48961
Rotation velocity of ball(r/min)	228100	240172
Revolution velocity of cage(r/min)	47660	47950

Table 3: Three different conditions.

operating condition	constant operating condition	constant operating condition
F_a=1000:500:3000 N	F_r=400N	ni=120000r/min
F_r=1000:100:1500N	F_a=1000N	ni=100000r/min
ni=100000:10000:140000r/min	F_a=2500N	F_r=400N

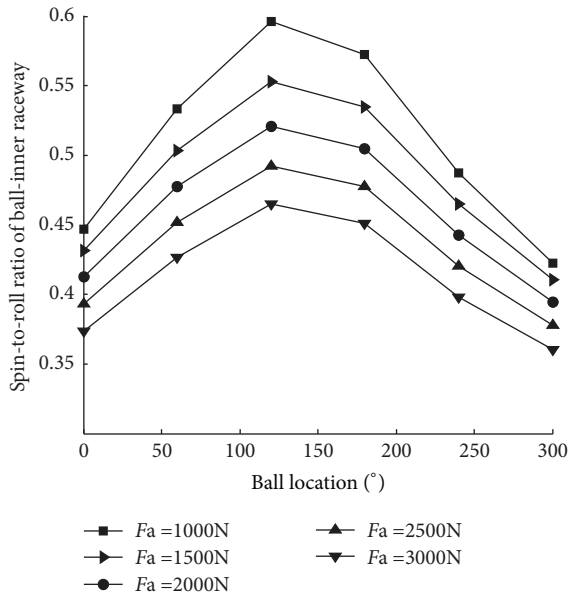

Figure 8: Spin-to-roll ratio of ball and inner raceway under different F_a.

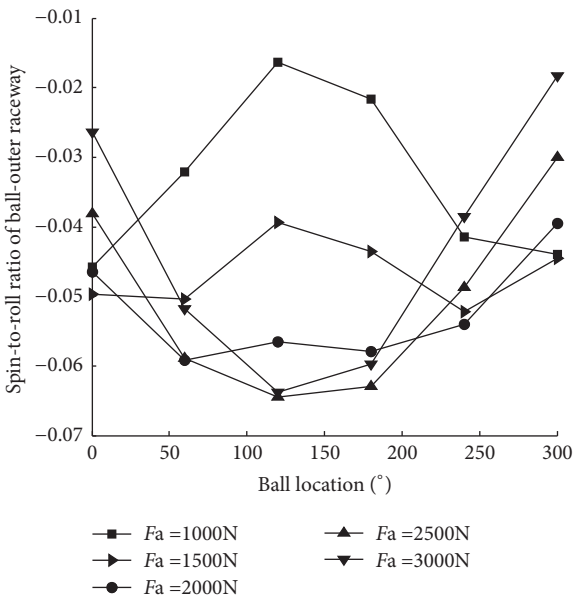

Figure 9: Spin-to-roll ratio of ball and outer raceway under different F_a.

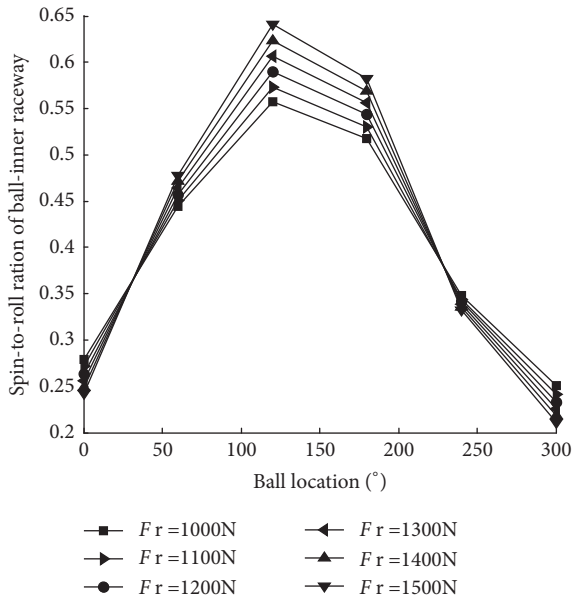

Figure 10: Spin-to-roll ratio of ball and inner raceway under different F_r.

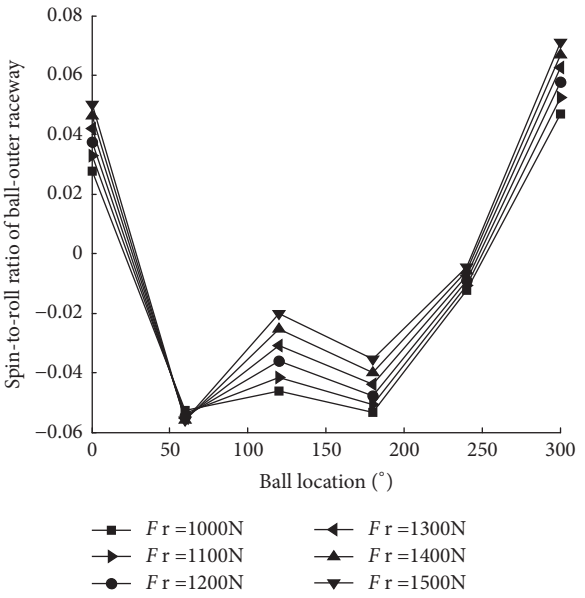

Figure 11: Spin-to-roll ratio of ball and outer raceway under different F_r.

reason for this phenomenon is that the ball at location angle of 120° is affected by the maximum centrifugal force.

4.1.2. Influence of Working Conditions on ω_{by}. Figure 14 shows the ω_{by} curves in the direction of y-axis in the azimuth coordinate system with the change of F_a. Under the condition load F_r and the constant rotational speed ni, ω_{by} gradually increases with F_a increasing. When F_a=3000 N, ω_{by} is basically stable at any ball azimuth location. Such phenomena suggest that *Fa* can reduce the axial clearance and decrease the influence of F_r on the ball, and the load condition of the ball tends to be steady.

The changing curves of ω_{by} along y-axis in the azimuth coordinate system with the change of F_r are shown in Figure 15. It can be illustrated that when F_a and ni are constant, ω_{by} gradually decreases with the increase of F_r, which is larger in the loading area. Such phenomena are due to the fact that F_r can reduce the radial clearance and inhibits the gyroscopic motion between the ball and the raceway and typically lead to ω_{by} decreasing significantly in loading area.

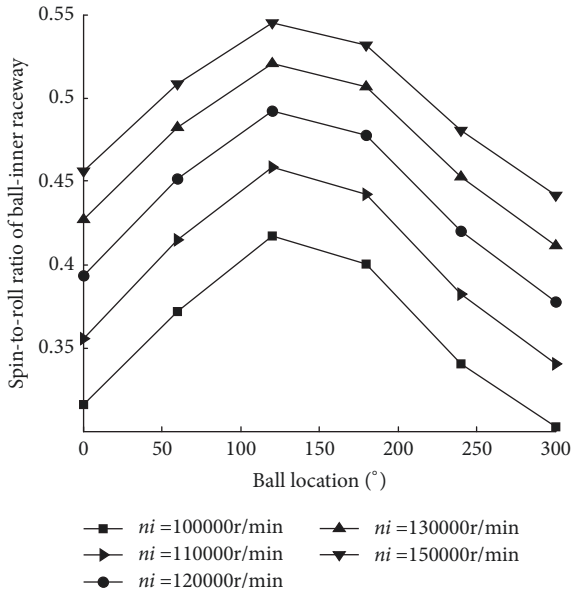

Figure 12: Spin-to-roll ratio of ball and inner raceway with different *ni*.

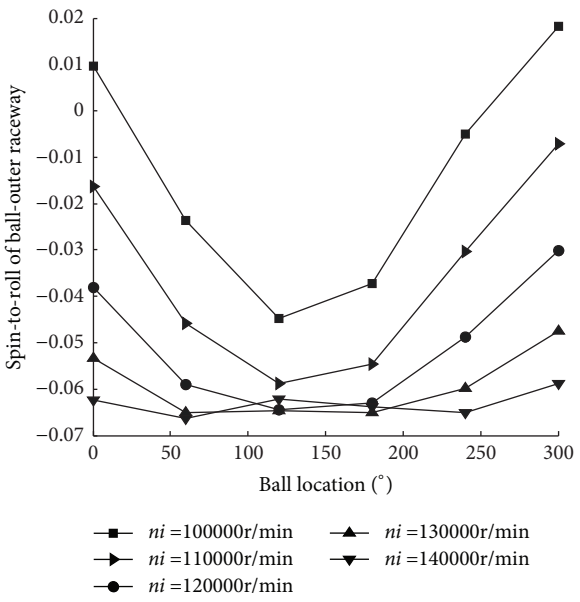

Figure 13: Spin-to-roll ratio of ball and outer raceway with different *ni*.

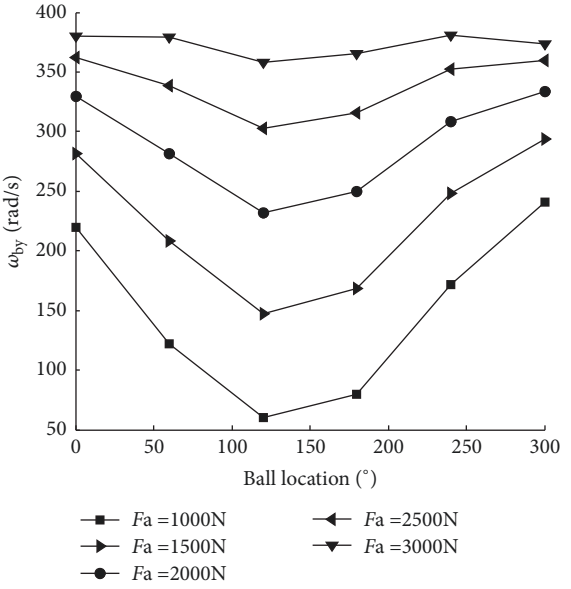

Figure 14: ω_{by} curves under different F_a.

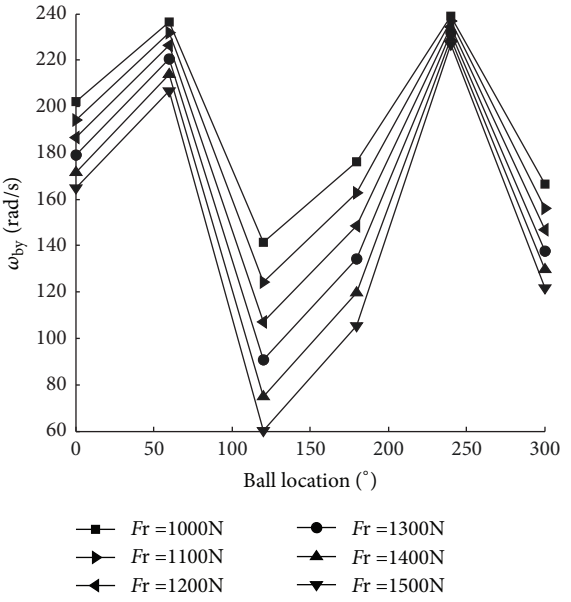

Figure 15: ω_{by} curves under different F_r.

As shown in the Figure 16 of ω_{by} changing curves with the change of *ni*, under the constant load F_a and F_r, the value of ω_{by} gradually increases with *ni* increasing, and the ω_{by} of the ball varies obviously with different ball azimuth location. ω_{by} increases slowly with the increase of *ni* in the loading area, whereas the increase is obvious in nonloading areas. Such phenomena are due to the fact that the radial load holds the ball and the raceway tight in the loading area and inhibits the changes of the ball in the space position, which causes ω_{by} increasing slowly. When *ni* is greater than 110000r/min, at location angle of 120°, the ω_{by} value of the ball reaches the minimum. The reason for this phenomenon is that the ball at this position bear the maximum load because of radial load F_r, and the increased centrifugal force compacts the ball and the raceway, resulting in the minimum ω_{by} here.

4.2. Influence of Working Conditions on Cage

4.2.1. Cage Forces. There exits three types of interaction conditions between the ball and the pocket of cage, such as (i) the pocket colliding the balls, (ii) the balls colliding the pocket, and (iii) no contact between the ball and the pocket. In order to study the relative motions between the ball and the

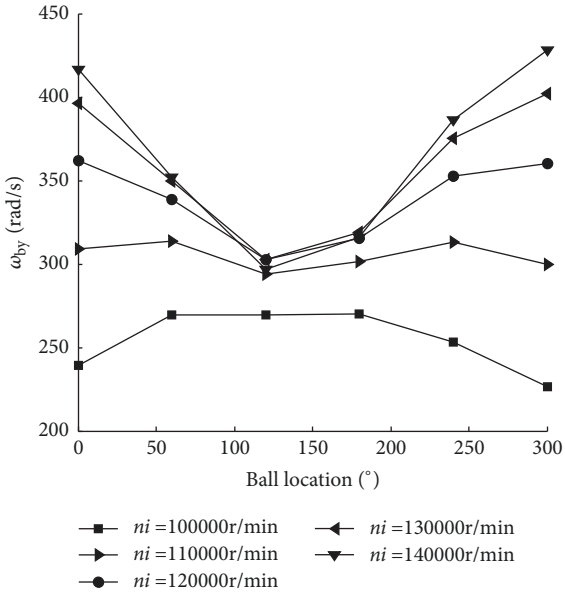

Figure 16: ω_{by} curves with different ni.

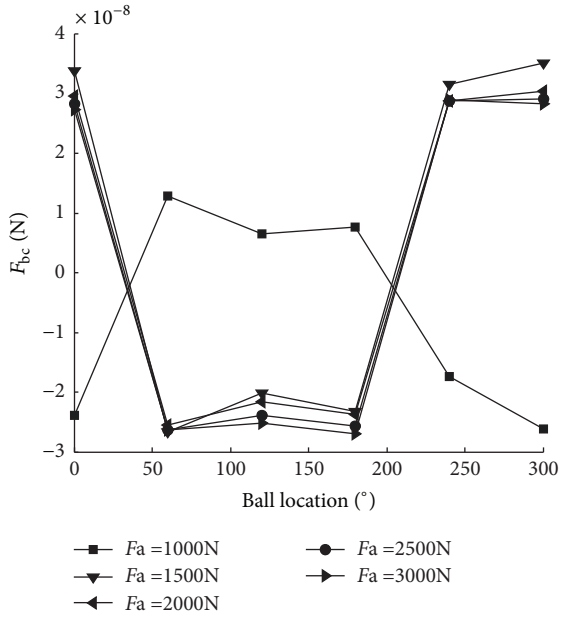

Figure 17: F_{bc} curves under different F_a.

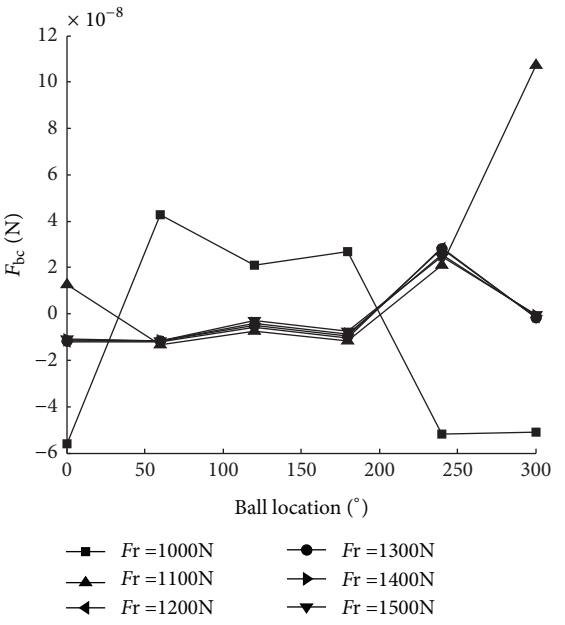

Figure 18: F_{bc} curves under different F_r.

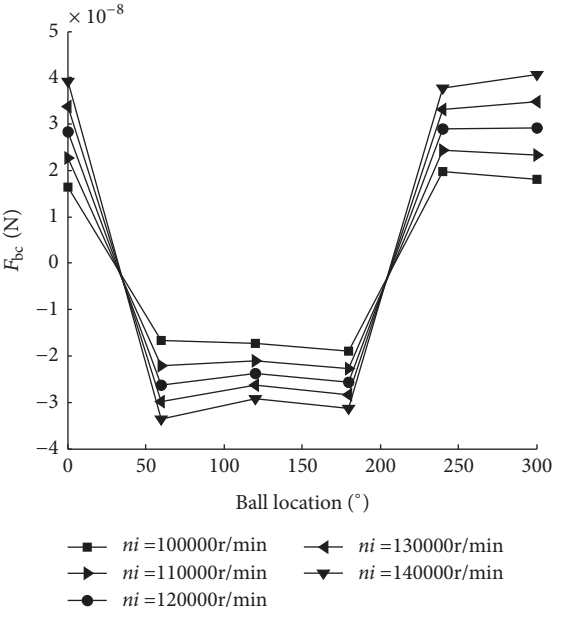

Figure 19: F_{bc} curves under different ni.

pocket, the three working condition as tabulated in Table 2 were analyzed.

Figures 17–19 illustrate the F_{bc} curves between the ball and the pocket of cage with different F_a, F_r, and ni. In these Figures, the negative value represents the pocket colliding the ball and conversely the positive is the ball colliding the pocket. (i) It can be illustrated that the normal load between the ball and the pocket of cage is very small during the steady-state working period; (ii) the ball and the pocket collide with each other. It will last until the dynamic equilibrium state is achieved during the bearing steady working state. (iii) Figure 19 shows that as ni increases, the normal load between the cage and the ball gradually decreases in the loading area. The reason for this phenomenon is that the centrifugal force increases with ni increasing in the loading area; it leads to the fact that the ball and the raceway are compressed; and the result is that the ball rotation angular velocity decreases, making the contact force between the ball and the cage decrease. In no-load areas, the opposite is true.

4.2.2. Cage Rotation Speed. In this paper, the relationship between the cage rotational angular speed and the ball

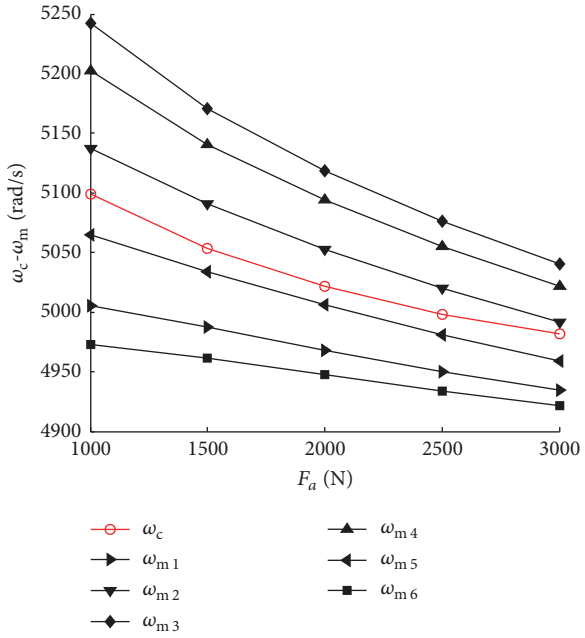

Figure 20: ω_c and ω_m curves with different F_a.

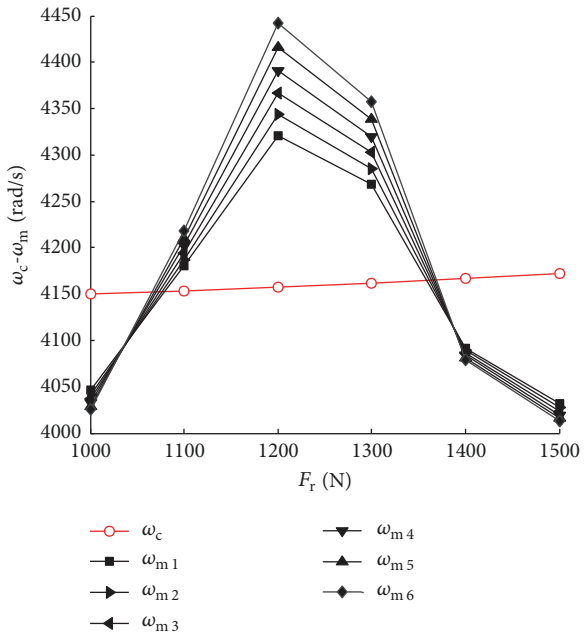

Figure 21: ω_c and ω_m curves with different F_r.

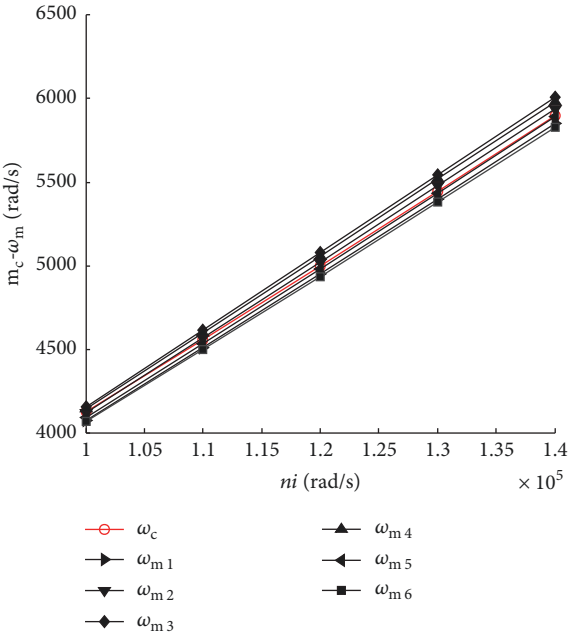

Figure 22: ω_c and ω_m curves with different ni.

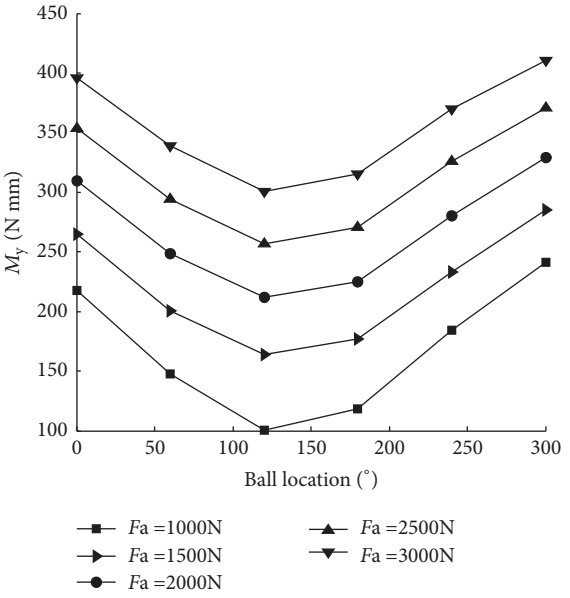

Figure 23: M_y curves with different F_a.

revolution angular speed is studied from the three working conditions listed in Table 2.

ω_c and ω_m curves of with different F_a, F_r, and ni are shown in Figures 20–22, which suggest that ω_c and ω_m decrease with the increase of F_a, and increase with the increase of ni, while the change of F_r has little effect on ω_c and ω_m. The value of ω_c lies in the middle position of the values of ω_m. Therefore, it is reasonable to take the average speed value of the balls as the cage rotational angular speed.

4.3. Influence of Working Conditions on Gyroscopic Moment. The gyroscopic moment is a dynamic inertial force produced during the process of bearing operation, which is harmful for the bearing operation condition. Especially, under the condition of high speed and light load, it causes the sliding, which will lead to serious friction, makes the bearing internal fever, heats up, and accelerates the bearing degeneration.

Figures 23 and 24 show the curves of M_y and M_z with the change of F_a. Under the constant values of F_r and ni, (i) M_y and M_z increase obviously with the increase of Fa, (ii) when F_a=3000 N, M_z tends to be stable at each ball azimuth

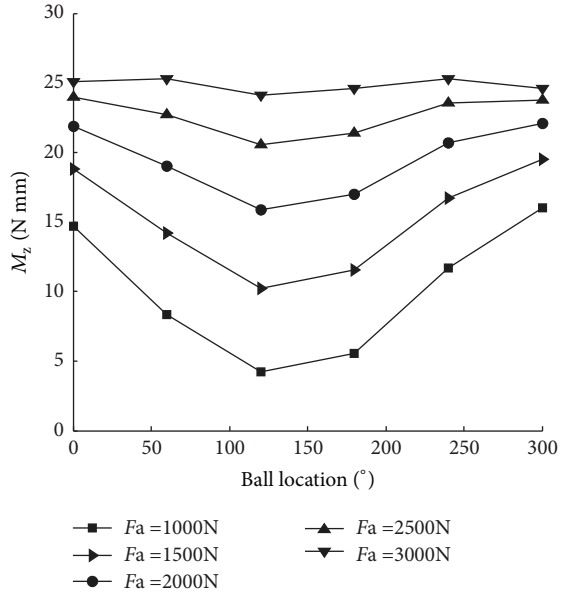

Figure 24: M_z curves with different F_a.

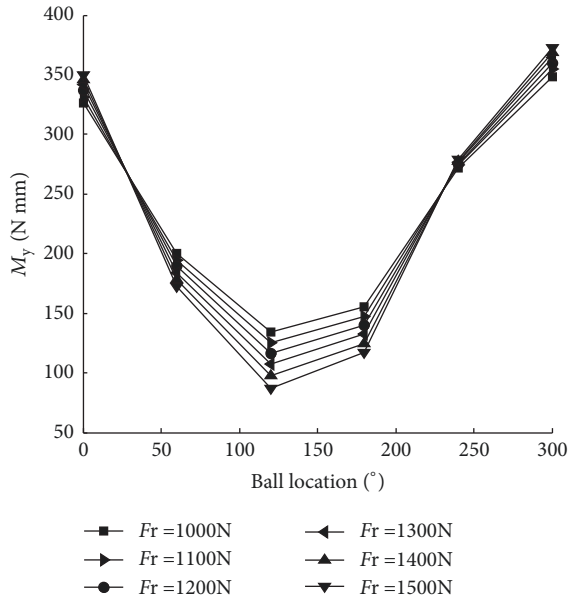

Figure 25: M_y curves with different F_r.

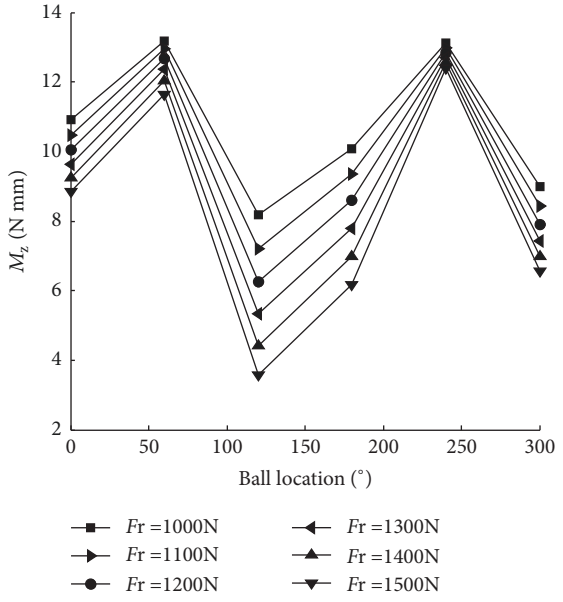

Figure 26: M_z curves with different F_r.

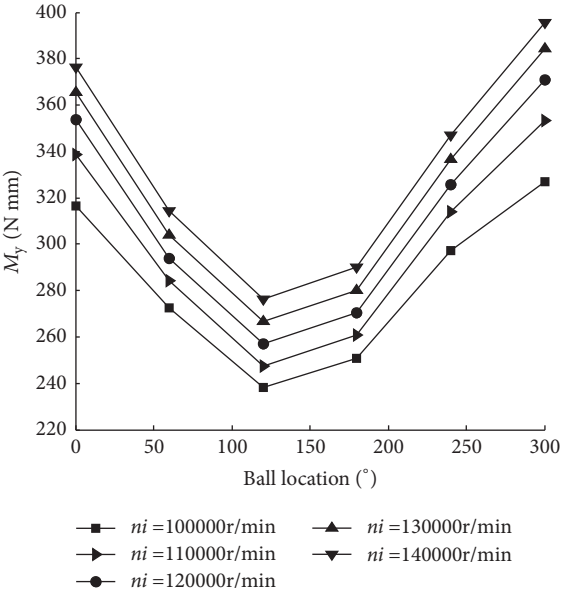

Figure 27: M_y curves with different ni.

location. Such phenomena are due to the fact that Fa reduces the axial clearance and the impact of F_r on balls and results in the same load condition for balls.

Figures 25 and 26 show the curves of M_y and M_z with the change of F_r. Under the constant values of F_a and ni, M_y and M_z gradually decrease with the increase of F_r. It is because that the increase of F_r will decrease the radial clearance of the bearing; therefore, the rolling body and the ring are pressed tightly, and the gyroscopic moment is suppressed and reduced.

Figures 27 and 28 show the curves of M_y and M_z with the change of ni in the direction of y and z of the azimuth coordinate system of the ball. It is illustrated that M_y and M_z increase significantly with the increase of ni under the constant load of F_a and F_r.

5. Conclusions

(1) The change of F_a, F_r, and ni can affect the spin-to-roll ratio of ball-inner raceway and ball-outer raceway. In different working conditions, the spin-to-roll ratio of the ball-inner raceway is greater than that of the ball-outer raceway. In high speed, the outer raceway control hypothesis is only a special case. In general,

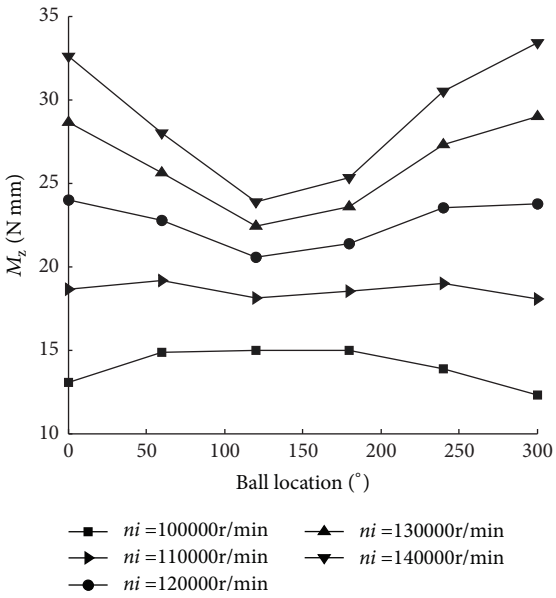

Figure 28: M_z curves with different *ni*.

there is a spin angular velocity between the ball and the outer raceway.

(2) The increase of F_a and *ni* of spindle bearing can cause ω_{by} increase; however, the increase of F_r will cause ω_{by} decrease. A specific F_a can reduce the axial clearance of the bearing, which will make the azimuth of the ball tend to be stable in the space.

(3) The interaction between the ball and the pocket of cage is that not only does the ball collide with the pocket but also the pocket collides with the ball, which can achieve the dynamic equilibrium state of the bearing steady-state work.

(4) It is reasonable to take the average speed value of the balls as the cage rotational angular speed.

(5) Gyroscope moment increases significantly with the increase of F_a and *ni*. The increase of F_r can suppress the gyroscopic movement.

Nomenclature

O_XYZ: Inertial coordinate system
O_xyz: Coordinate system
a: Contact angle (°)
α: Semimajor axis of the contact area (mm)
b: Semiminor axis of the contact area (mm)
β: Spiral angle (°)
β': Yaw angle (°)
D_m: Pitch diameter (mm)
F: Hertz contact force (N)
F_a: Thrust load (N)
F_r: Radial load (N)
F_{bc}: Force act on cage by ball (N)
f: Groove curvature radius coefficient
G: Dimensionless material parameters
h: Center oil film thickness (mm)
h_0: Central oil film thickness (mm)
I_b: The inertia moment of ball
J: Inertia moment
K: Hertz contact stiffness coefficients
m: Quality (kg)
M_y: The gyroscopic moment along z-axis in the azimuth coordinate system of ball (N.mm)
M_z: The gyroscopic moment along y-axis in the azimuth coordinate system of ball (N.mm)
ni: The inner ring rotational speed (r/min)
$\boldsymbol{r}$: Displacement vector
R: Radius (mm)
ρ: Density (g/cm^3)
ρ_{oa}: Density of the mixture gas (g/cm^3)
T: Tangential force (N)
ω: Angular speed (rad/s)
ω_c: The cage rotational angular velocity (rad/s)
ω_m: The ball revolution angular velocity (rad/s)
ω_{by}: The ball rotation angular velocity along y-axis in the azimuth coordinate system of ball(rad/s)
v_r: Relative sliding velocity (m/s)
δ: Elastic approach (mm)
θ: Relative angular displacement (°)
μ: Friction coefficient.

Superscript

a: The azimuth coordinates of the ball
r: The fixed body coordinate system of inner ring
i: Inertial coordinate
c: The fixed body coordinate system of the cage
p: The pocket coordinate
g: Contact coordinate.

Subscript

b: Ball
i: Inner ring
e: Outer ring
c: Cage
p: Cage pocket
g: Contact point
j: The jth ball
x, y, z: The coordinate components.

Data Availability

The data used to support the findings of this study are available from the corresponding author upon request.

Conflicts of Interest

The authors confirm that article content has no conflicts of interest.

Acknowledgments

This work was supported by the National Natural Science Foundation of China (no. 51805299), Shandong High School Research Project (J18KA004), and the subtopic of the program in the field of Intelligent Manufacturing and Advanced Materials, Scientific and Technological Innovation Plan (no. 13521103002) in Shanghai University.

References

[1] L. Houpert, "CAGEDYN: a contribution to roller bearing dynamic calculations. Part III: experimental validation," *ASME Tribology Transactions*, vol. 53, no. 6, pp. 848–859, 2010.

[2] S. Creju, I. Bercea, and N. Mitu, "A dynamic analysis of tapered roller bearing under fully flooded conditions part 1: theoretical formulation," *Wear*, vol. 188, no. 1-2, pp. 1–10, 1995.

[3] I. Bercea, S. Cretu, and D. Nélias, "Analysis of double-row tapered roller bearings, part i - model," *Tribology Transactions*, vol. 46, no. 2, pp. 228–239, 2003.

[4] T. A. Harris, *Rolling Bearing Analysis*, John, New York, 5th edition, p. 44, 2001.

[5] Y. L. Ru, *Quasi-Dynamic Analysis of High Speed Roller Bearings Mechanicalence & Technology*, 1995.

[6] L. Wang and Y. Li, "Boundary for aviation bearing accelerated life test based on quasi-dynamic analysis," *Tribology International*, vol. 116, pp. 414–421, 2017.

[7] G. Z. Ren, Z. X. Liu, and W. J. Gao, "Research on Dynamic Behaviors of Counter-Rotating Cylindrical Roller Bearing Based on Quasi-Dynamic Method," *Journal of Propulsion Technology*, 2016.

[8] D.-S. Li, G.-D. Chen, and Y.-J. Yu, "Analysis on dynamic characteristics of high speed angular contact ball bearing based on quasi-dynamic," *Hangkong Dongli Xuebao/Journal of Aerospace Power*, vol. 32, no. 3, pp. 730–739, 2017.

[9] O. Özşahin, H. N. Özgüven, and E. Budak, "Analytical modeling of asymmetric multi-segment rotor - Bearing systems with Timoshenko beam model including gyroscopic moments," *Computers & Structures*, vol. 144, pp. 119–126, 2014.

[10] G. H. Jang and S. W. Jeong, "Analysis of a ball bearing with waviness considering the centrifugal force and gyroscopic moment of the ball," *Journal of Tribology*, vol. 125, no. 3, pp. 487–498, 2003.

[11] T. Hu, G.-F. Yin, and M.-N. Sun, "Dynamic performance of a shaft-bearing system with centrifugal force and gyroscopic moment effects," *Zhendong yu Chongji*, vol. 33, no. 8, pp. 100–108, 2014.

[12] K. Yan, Y. Wang, Y. Zhu, J. Hong, and Q. Zhai, "Investigation on heat dissipation characteristic of ball bearing cage and inside cavity at ultra high rotation speed," *Tribology International*, vol. 93, pp. 470–481, 2015.

[13] M. P. Rivera, "Bearing-cage frictional instability—a mechanical model," *Tribology Transactions*, vol. 34, no. 1, pp. 117–121, 1991.

[14] S. Kerst, B. Shyrokau, and E. Holweg, "A semi-analytical bearing model considering outer race flexibility for model based bearing load monitoring," *Mechanical Systems and Signal Processing*, vol. 104, pp. 384–397, 2018.

[15] P. K. Gupta and N. H. Forster, "Modeling of Wear in a Solid-Lubricated Ball Bearing," *A S L E Transactions*, vol. 30, no. 1, pp. 55–62, 1987.

[16] D. E. Brewe, B. J. Hamrock, and C. M. Taylor, "Effect of Geometry on Hydrodynamic Film Thickness," *Journal of Lubrication Technology*, vol. 101, no. 2, pp. 231–239, 1979.

[17] Y. P. Chiu, "A Theory of Hydrodynamic Friction Forces in Starved Point Contact Considering Cavitation," *Journal of Lubrication Technology*, vol. 96, no. 2, pp. 237–245, 1974.

[18] A. Cameron, *Fundamentals of lubrication theory*, China Machine Press, Beijing, 1th edition, 1980.

[19] T. A. Harris and M. H. Mindel, "Rolling element bearing dynamics," *Wear*, vol. 23, no. 3, pp. 311–337, 1973.

[20] V. Streeter, *Fluid Mechanics*, Mcgraw-Hill, New York, NY, USA, pp. 313-314, 1951.